

Optics Letters

Temperature-decoupled hydrogen sensing with Pi-shifted fiber Bragg gratings and a partial palladium coating

FABIAN BUCHFELLNER,^{1,*} QIANG BIAN,^{1,2} WENBIN HU,³ XIANGYANG HU,³ MINGHONG YANG,³ ALEXANDER W. KOCH,² AND JOHANNES ROTH¹

¹Photonics Lab, Munich University of Applied Sciences, 80335 Munich, Germany

²Institute for Measurement Systems and Sensor Technology, Technical University of Munich, 80333 Munich, Germany

³National Engineering Research Center for Optical Fiber Sensing Technology, Wuhan University of Technology, 430070 Wuhan, China

*Corresponding author: fabian.buchfeller0@hm.edu

Received 9 September 2022; revised 29 November 2022; accepted 29 November 2022; posted 29 November 2022; published 20 December 2022

A novel, to the best of our knowledge, sensor architecture for palladium-coated fiber Bragg gratings is proposed and demonstrated that allows highly accurate multi-parameter sensing and decoupling of hydrogen concentration from temperature. By means of partly Pd-coated Pi-shifted FBGs (PSFBGs), the notch wavelength of the narrow transmission band and the flank wavelength of the broader reflection band experience different hydrogen and temperature sensitivities. PSFBGs were calibrated at hydrogen concentrations between 800 and 10,000 ppm and temperatures from 20 to 40°C, and a decreased hydrogen sensitivity at increased temperatures was found. Nonlinear temperature-dependent hydrogen calibration functions were therefore determined. An iterative matrix algorithm was used to decouple hydrogen concentration and temperature and to account for the nonlinear calibration functions. Achieved improvements and results have great importance for real field applications of FBG-based hydrogen sensing. © 2022 Optica Publishing Group

<https://doi.org/10.1364/OL.474083>

Reduction of environmental pollution and technological progress in energy production, storage, and mobility necessitates a blending or total substitution of fossil fuels with alternative renewable energy sources [1]. Hydrogen has been identified as a promising candidate, although safety concerns emerged rapidly due to its low ignition energy, high diffusivity, and particularly its large flammable range of 4–75% by volume in air [2].

In the group of optical hydrogen sensors, free space [3,4] or fiber optic [5] solutions, such as interferometric [6] or grating-based [7] devices have been reported. Fiber Bragg gratings (FBGs) are promising candidates for hydrogen detection with an intrinsic safety in explosion endangered areas and capability for upscaling to large numbers of sensors per fiber and interrogation unit due to wavelength-division multiplexing.

Functionalization of FBGs for hydrogen sensing can be achieved with thin palladium (Pd) or Pd alloy films covering the

optical fiber at the grating location [8]. At the Pd surface, molecular hydrogen dissociates into atomic hydrogen and diffuses into the bulk, where PdH_x hybrids are formed. This formation causes lattice strains in the Pd layers [9]. Coupling these strains into the fiber leads to wavelength shifts of the FBG as a function of hydrogen concentration [8]. Counterproductively, temperature-induced wavelength shifts typically distort the hydrogen signals severely due to the intrinsic temperature sensitivity of FBGs. Moreover, the solubility of hydrogen in Pd shows an inverse proportionality to temperature [10], i.e., increasing temperatures reduce the total number of dissolvable hydrogen atoms, leading to reduced hydrogen sensitivity. Deploying FBG-based hydrogen sensors in field applications with requirements for large temperature ranges of −20 to +50°C [2] is therefore hardly feasible without compensation for temperature. Hence, robust and accurate methods are required to decouple temperature and hydrogen concentration and to obtain fast and reliable FBG-based hydrogen detection. Reported solutions in the literature contained temperature stabilization, e.g., with in-fiber optical heating [11], or utilization of tilted FBGs, where cladding modes can be referenced to the core mode to reduce temperature cross-sensitivity [7]. Temperature compensation with external FBG temperature sensors was also reported [12]. However, a slight positioning error can have serious impact, especially for free gas flows with temperature gradients arising from leakages. Multi-parameter sensing with FBGs has been previously reported [13], e.g., to compensate friction-induced forces during temperature measurements [14], for strain-compensated temperature measurements with surface-glued polarization-maintaining fibers [15], and for simultaneous force and temperature sensing with laser-machined micro-structured FBGs [16].

This Letter proposes and demonstrates a multi-parameter fiber optic hydrogen sensor with *in situ* temperature compensation by means of Pi-shifted FBGs (PSFBGs) and partly Pd-coated gratings. PSFBGs have a phase shift of π in the center of their periodic refractive index modulation $n(z)$, as shown in Fig. 1(a). Correspondingly, the reflection spectra of PSFBGs feature a

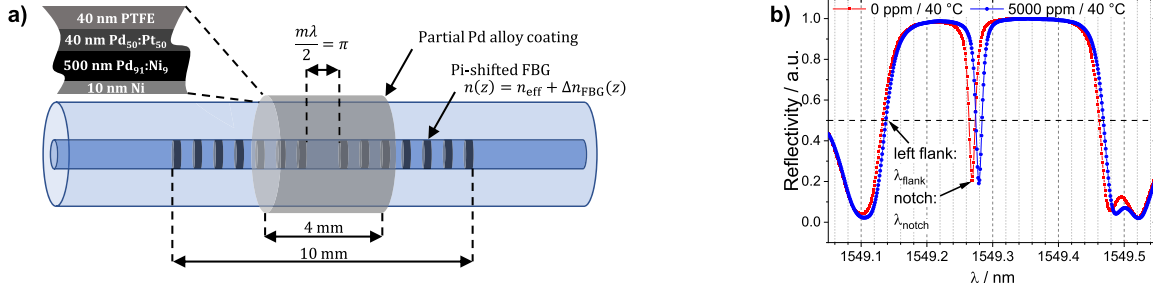


Fig. 1. (a) Schematic of a partly Pd-coated Pi-shifted FBG hydrogen sensor. (b) Spectra of a partly Pd-coated Pi-shifted FBG at 40°C and at hydrogen concentrations of 0 ppm (red) and 5000 ppm (blue).

narrow transmission notch within a broader reflection band, as shown in Fig. 1(b).

Only a small 4-mm-long section of the 10-mm-long FBG at the location of the Pi shift is coated with Pd [see Fig. 1(a)]. The sensor principle can be explained more easily under the simplifying assumption that the Pd-coated length is much smaller than the total length of the FBG. With this assumption, the enveloping reflection spectrum of the pi-shifted FBG is still affected by temperature but almost independent of the hydrogen concentration. However, hydrogen induces strains in the Pd and thus in a small section of the fiber at the location of the phase shift. These strains will change the spacing of the phase shift and hence shift the position of the notch relative to the entire reflection spectrum. In this simplified view, the temperature can be measured by evaluating the position of the envelope reflection spectrum, as represented by λ_{flank} [see Fig. 1(b)], and the hydrogen concentration can be determined by evaluating the separation between λ_{flank} and λ_{notch} .

In reality, λ_{flank} will also be influenced by hydrogen to some extent, and the separation of λ_{flank} and λ_{notch} also depends on temperature due to the temperature-dependence of the hydrogen solubility in Pd and the thermal expansion of Pd. To take these effects fully into account, an iterative matrix algorithm (IMA) was used. This approach was first proposed for FBG-based multi-parameter measurements by Hopf *et al.* [14]. They applied this method for simultaneous measurement of force and temperature using a nearby pair of FBGs in fibers with different diameters, and achieved improved accuracy as the nonlinear temperature dependence could be included, and friction-induced forces were decoupled. Here, the IMA is used to consider the nonlinearity and the temperature dependence of the hydrogen sensitivity. This approach, using a PSFBG in combination with a partial Pd coating, allows the measurement of both quantities at exactly the same position, which practically excludes any temperature gradient between the sensing points of temperature and hydrogen, and hence optimizes accuracy.

The centered 4 mm of the grating were covered by a 4-layer thin film including a pure nickel (Ni) adhesion layer (10 nm), a Pd₉₁Ni₉ sensitive layer (500 nm), a Pd₅₀Pt₅₀ catalytic layer (40 nm), and a PTFE protection layer (40 nm) [see Fig. 1(a)]. While pure Pd suffers from hysteresis at even low concentrations, the alloying of the sensitive layer with Ni shifts the hysteretic region to higher concentrations, making the sensor usable for hysteresis-free detection at low concentrations [17]. Further details on the binary material sputtering process of the Pd alloys are given in [12]. The parameters were chosen arbitrarily for a proof-of-concept, while further optimization is subject

to upcoming experiments. Spectra were acquired with a FAZT I4G interrogator (Optics11, Amsterdam, Netherlands), having a spectral resolution of 1 pm and an acquisition rate of 4 Hz. Figure 1(b) shows two spectra of the PSFBG with partial Pd coating, both taken at a temperature of 40°C. The red data show the spectrum without any hydrogen, while the blue spectrum was measured at a hydrogen concentration, c , of 5000 ppm. Figure 1(b) indicates that the notch wavelength has shifted slightly more than the flank wavelength.

The IMA developed by Hopf *et al.* [14] requires two measurands, which were chosen here as the shift of the left flank wavelength, $\Delta\lambda_{flank}$, and the shift of the separation between flank and notch wavelength, $\delta\lambda$. The flank wavelength shift, $\Delta\lambda_{flank}(\vartheta, c)$, can be expressed as

$$\Delta\lambda_{flank}(\vartheta, c) = \lambda_{flank}(\vartheta, c) - \lambda_0(0, 0) \quad (1)$$

$$= \Delta\lambda_{flank,\vartheta}(\vartheta) + \Delta\lambda_{flank,c}(\vartheta, c), \quad (2)$$

where λ_0 denotes the reference wavelength at 0°C and 0 ppm, $\Delta\lambda_{flank,\vartheta}(\vartheta)$ denotes the temperature-induced wavelength shift, and $\Delta\lambda_{flank,c}(\vartheta, c)$ the temperature-dependent hydrogen-induced wavelength shift. The notch wavelength shift, $\Delta\lambda_{notch}(\vartheta, c)$, can be defined similarly. The shift of the separation between flank and notch, $\delta\lambda(\vartheta, c)$, is given by

$$\delta\lambda(\vartheta, c) = \Delta\lambda_{notch}(\vartheta, c) - \Delta\lambda_{flank}(\vartheta, c) \quad (3)$$

$$= \delta\lambda_{\vartheta}(\vartheta) + \delta\lambda_c(\vartheta, c), \quad (4)$$

where $\Delta\lambda_{notch}(\vartheta, c)$ and $\Delta\lambda_{flank}(\vartheta, c)$ are the notch and flank wavelength shifts due to hydrogen and temperature, and $\delta\lambda_{\vartheta}(\vartheta)$ is the temperature-induced and $\delta\lambda_c(\vartheta, c)$ is the temperature-dependent hydrogen-induced change of the spectral distance. The sensitivity matrix $\mathbf{S}(\vartheta, c)$ can be expressed as

$$\begin{pmatrix} \Delta\lambda_{flank}(\vartheta, c) \\ \delta\lambda(\vartheta, c) \end{pmatrix} = \begin{bmatrix} K_{\Delta\lambda_{flank,\vartheta}}(\vartheta) & K_{\Delta\lambda_{flank,c}}(\vartheta, c) \\ K_{\delta\lambda_{\vartheta}}(\vartheta) & K_{\delta\lambda_c}(\vartheta, c) \end{bmatrix} \begin{pmatrix} \vartheta \\ c \end{pmatrix}, \quad (5)$$

where $K_{\Delta\lambda_{flank,\vartheta}}(\vartheta)$, $K_{\delta\lambda_{\vartheta}}(\vartheta)$ are the nonlinear temperature sensitivities of the two measurands and $K_{\Delta\lambda_{flank,c}}(\vartheta, c)$, $K_{\delta\lambda_c}(\vartheta, c)$ the nonlinear temperature-dependent hydrogen sensitivities.

Temperature calibration from 10 to 60°C of both measurands, $\Delta\lambda_{flank,\vartheta}(\vartheta)$ and $\delta\lambda_{\vartheta}(\vartheta)$, was performed with a Peltier-driven temperature-stabilized unit according to the procedure reported in [18]. Parabolic temperature calibration functions were fitted to the calibration data to obtain calibration coefficients and quantities for the temperature sensitivities $K_{\Delta\lambda_{flank,\vartheta}}(\vartheta)$, $K_{\delta\lambda_{\vartheta}}(\vartheta)$.

Hydrogen calibration at different temperatures was performed using a flow-through apparatus, as schematically shown in Fig. 2.

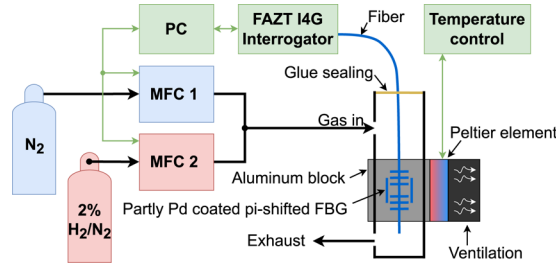


Fig. 2. Hydrogen calibration setup with mass flow controllers (MFCs) to mix pure N₂ with pre-mixed H₂/N₂. Temperature stabilization was realized with a Peltier element and data were acquired with a FAZT I4G (Optics11) interrogator.

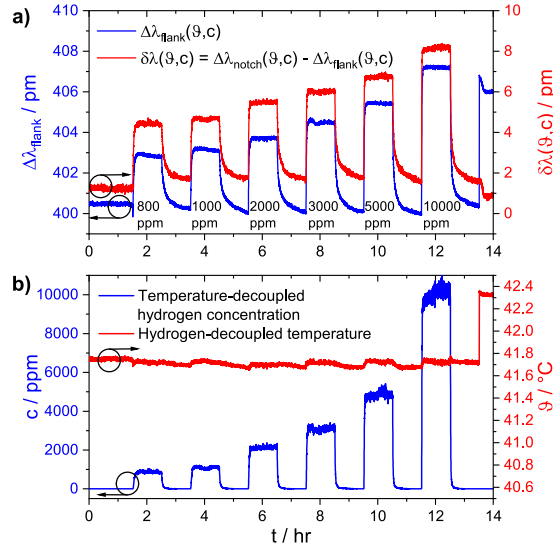


Fig. 3. Hydrogen calibration cycles of (a) the flank wavelength shift, $\Delta\lambda_{flank}$ (blue, left ordinate), and the shift of the separation between the flank and notch wavelength, $\delta\lambda$ (red, right ordinate), and (b) the temperature-decoupled hydrogen concentration (blue, left ordinate) and the hydrogen-decoupled temperature (red, right ordinate) calculated with the IMA.

The desired hydrogen concentration was controlled using two mass flow controllers (MFCs) that mixed pure nitrogen with pre-mixed 2 vol.% H₂/N₂ at a flow rate of 500 sccm. Six hydrogen concentration set points, as denoted in Fig. 3(a), between 800 and 10,000 ppm with a dwell time of 1 h were set with an accuracy of $\pm 1\%$ of the full scale. At the PSFBG's position, the tubes were surrounded by an aluminum block, and a Peltier element provided temperature stabilization of the tubes. Hydrogen calibrations were performed at 20°C, 30°C, and 40°C.

As an example, the time series of the hydrogen calibration at 40°C is shown in Fig. 3(a) for $\Delta\lambda_{flank}(\theta, c)$ (blue, left ordinate) and $\delta\lambda(\theta, c)$ (red, right ordinate). Baselines of both signals, as found at $t < 1.5$ h, were stable as expected due to the temperature control. At each temperature, $\delta\lambda(\theta, c)$ and $\Delta\lambda_{flank}(\theta, c)$ were measured at six hydrogen concentration levels ranging from 800 to 10,000 ppm. Data taken at saturation levels were averaged and plotted in Figs. 4(a) and 4(c) as functions of hydrogen concentrations given by the MFCs. Colors indicate the three different calibration temperatures. As aforementioned, the solubility of hydrogen in Pd decreases with increasing temperature [10], and

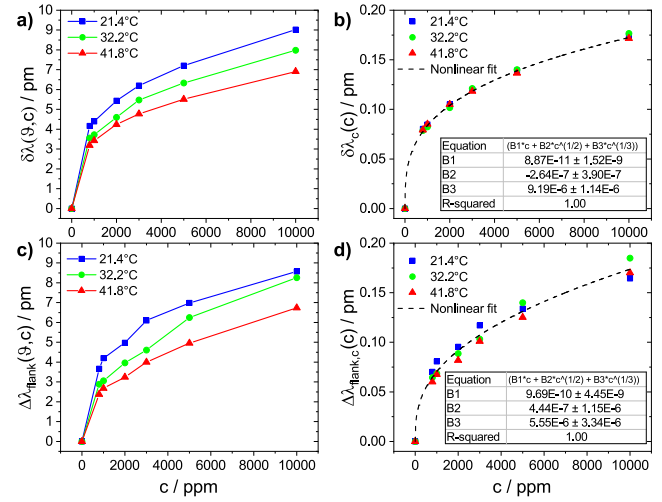


Fig. 4. Temperature-dependent hydrogen calibration results of (a) $\delta\lambda(\theta, c)$ and (c) $\Delta\lambda_{flank}(\theta, c)$. Temperature-compensated hydrogen calibration data for (b) $\delta\lambda_c(c)$ and (d) $\Delta\lambda_{flank,c}(c)$ with nonlinear fits (dashed lines).

the observed PSFBG's hydrogen sensitivity decreased from 20 to 40°C.

Nonetheless, it is desirable to find a generalized, temperature-compensated hydrogen calibration function, instead of finding functions for each temperature. Hence, we calculated the temperature-compensated hydrogen calibration data for the two measurands according to

$$\Delta\lambda_{flank,c}(c) = \exp\left[-\frac{\Delta H^0}{2R(\theta + 273)}\right] \Delta\lambda_{flank}(\theta, c), \quad (6)$$

$$\delta\lambda_c(c) = \exp\left[-\frac{\Delta H^0}{2R(\theta + 273)}\right] \delta\lambda(\theta, c), \quad (7)$$

where $H^0 = 4620$ cal mol⁻¹ is the heat of dissolution, and $R = 1.987$ cal mol⁻¹ K⁻¹ is the gas constant. The exponential term is a function of temperature, describing the temperature-dependent solubility of Pd following the Arrhenius law [10]. It can be seen in Figs. 4(b) and 4(d) that for both measurands, $\delta\lambda(\theta, c)$ and $\Delta\lambda_{flank}(\theta, c)$, the temperature-compensated calibration data fit well to generalized temperature-compensated calibration functions. It was found that these functions can approximately be described with 3-term summations of root functions, given by

$$\Delta\lambda_{flank,c}^{cal\ function}(c) = \sum_{i=1}^3 B_{i,\Delta\lambda_{flank,c}} c^{1/i}, \quad (8)$$

$$\delta\lambda_c^{cal\ function}(c) = \sum_{i=1}^3 B_{i,\delta\lambda_c} c^{1/i}. \quad (9)$$

The fit coefficients $B_{i,\Delta\lambda_{flank,c}}$ and $B_{i,\delta\lambda_c}$ are listed in the insets of Figs. 4(b) and 4(d), and they represent the temperature-compensated calibration coefficients for the hydrogen response. The 3-term summation of the root functions was motivated by Sieverts' square root law of hydrogen dissolution in metals, which was extended to 3 terms to reduce residuals. The temperature-dependent sensitivities for the hydrogen concentration, $K_{\Delta\lambda_{flank,c}}(\theta, c)$ and $K_{\delta\lambda_c}(\theta, c)$, as required in Eq. (5), are

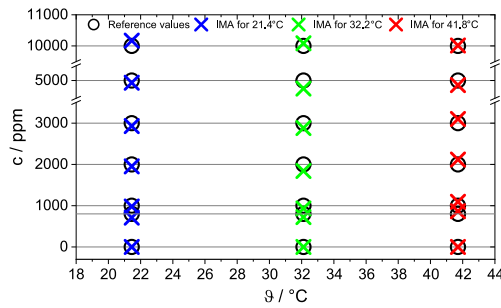


Fig. 5. Hydrogen concentration as a function of temperature. Comparison of reference values (circles) with data obtained by a procession with the IMA (crosses).

implicitly defined via the equations

$$\Delta\lambda_{flank,c}^{cal\ function}(c) = \exp\left[\frac{\Delta H^0}{2R(\theta + 273)}\right] \sum_{i=1}^3 B_{i,\Delta\lambda_{flank,c}} c^{1/i}, \quad (10)$$

$$= K_{\Delta\lambda_{flank,c}}(\theta, c) \times c, \quad (11)$$

$$\delta\lambda_c^{cal\ function}(c) = \exp\left[\frac{\Delta H^0}{2R(\theta + 273)}\right] \sum_{i=1}^3 B_{i,\delta\lambda_c} c^{1/i}, \quad (12)$$

$$= K_{\delta\lambda_c}(\theta, c) \times c. \quad (13)$$

After calibrations for temperature and hydrogen have been accomplished and their sensitivities for the measurands are identified, an inversion of the square matrix in Eq. (5) and the extension to a number of $j = 1 \dots N$ iterations gives [14]

$$\begin{pmatrix} \theta^j \\ c^j \end{pmatrix} = \frac{1}{\det[S(\theta, c)^{j-1}]} \quad (14)$$

$$\times \begin{bmatrix} K_{\delta\lambda_c}(\theta, c)^{j-1} & -K_{\Delta\lambda_{flank,c}}(\theta, c)^{j-1} \\ -K_{\delta\lambda_\theta}(\theta)^{j-1} & K_{\Delta\lambda_{flank,\theta}}(\theta)^{j-1} \end{bmatrix} \begin{pmatrix} \Delta\lambda_{flank} \\ \delta\lambda \end{pmatrix}. \quad (15)$$

Processed results after three iterations from the data of Fig. 3(a) are depicted in Fig. 3(b) for the temperature-decoupled hydrogen concentration (blue, left ordinate) and the hydrogen-decoupled temperature (red, right ordinate). A comparison of temperature-decoupled hydrogen concentration data [Fig. 3(b), blue] with the raw wavelength data [Fig. 3(a)] reveals that the sensor data quality improved significantly. The raw wavelength data show large time constants, but the sorption time constants in the temperature-decoupled hydrogen concentration were considerably lower. This can be explained by slight temperature variations, as the addition of hydrogen gas from another gas bottle than the pure N_2 slightly changed the gas temperature during hydrogen exposure, which can also be seen in the temperature data in Fig. 3(b). Hence, the large time constants in the raw wavelength data appeared due to both the hydrogen sorption in the Pd and the thermal stabilizing after a change in the gas flow. The remaining sorption time constants were in the range of over one minute. The present sensor configuration was not designed to achieve lower time constants, but this will be subject to further research. In addition, the baseline of the temperature-decoupled concentration signal always remained stable at ~ 0 during hydrogen absence, even at $t = 13.5$ h, where the gas flow was turned off and an immediate increase in temperature occurred. Without applying the IMA, this sharp temperature step would cause an indistinguishable wavelength shift of the raw wavelength data, where undesired temperature

effects would bias the hydrogen signal. In Fig. 5, a scatterplot shows the hydrogen concentration as a function of temperature for the hydrogen calibrations repeated at 20°C, 30°C, and 40°C. Circles indicate reference values read from the MFCs and absolute temperature calibration of $\Delta\lambda_{flank}$. Crosses indicate the decoupled values processed by the IMA. This result verifies that the partly Pd-coated PSFBG hydrogen sensor in combination with the IMA agrees well with reference data (concentration deviations < 100 ppm) over a relatively broad concentration and temperature range. The minimally tested concentration level was 800 ppm, although the time series in Fig. 3 shows a noise of ~ 300 fm, suggesting lower detection limits of < 200 ppm. We assume that the proposed temperature-decoupled hydrogen sensing method can be further improved in terms of sensitivity, e.g., by optimizing the coating composition and with reduced fiber diameters. Nonetheless, without decoupling of hydrogen and temperature, i.e., using the raw wavelength data as the signal, temperature fluctuations would dominate the measurement and make hydrogen sensing unfeasible for real-world applications. The proposed sensor combined with the multiplexing capability of fiber optics opens broad application fields such as concentration and temperature distribution measurements in electrolyzers or fuel cells, industrial process control, and hydrogen leakage detection of large areas and critical infrastructure.

Funding. Deutsche Forschungsgemeinschaft (448330062); National Natural Science Foundation of China (62061136002).

Disclosures. The authors declare no conflicts of interest.

Data availability. Data underlying the results presented in this paper are not publicly available at this time but may be obtained from the authors upon reasonable request.

REFERENCES

- European Commission, "The European Green Deal: Communication from the Commission," (2019).
- "Hydrogen detection apparatus - stationary applications," ISO 26142:2010-06.
- E. Herkert, F. Sterl, N. Strohfeldt, R. Walter, and H. Giessen, *ACS Sens.* **5**, 978 (2020).
- Y.-J. Chen, F.-C. Lin, A. K. Singh, L. Ouyang, and J.-S. Huang, *Adv. Opt. Mater.* **9**, 2100869 (2021).
- G. Wang, J. Dai, and M. Yang, *IEEE Sens. J.* **21**, 12706 (2021).
- J. Ma, Y. Zhou, X. Bai, K. Chen, and B.-o. Guan, *Nanoscale* **11**, 15821 (2019).
- S. Cai, F. Liu, R. Wang, Y. Xiao, K. Li, C. Caucheteur, and T. Guo, *Sci. China Inf. Sci.* **63**, 222401 (2020).
- B. Sutapun, *Sens. Actuators, B* **60**, 27 (1999).
- H. Peisl, *Hydrogen in metals* (Springer, Berlin, 1978), Topics in Applied Physics, pp. 53–74.
- J. D. Clewley, T. Curran, T. B. Flanagan, and W. A. Oates, *J. Chem. Soc., Faraday Trans. 1* **69**, 449 (1973).
- M. Buric, T. Chen, M. Maklad, P. R. Swinehart, and K. P. Chen, *IEEE Photonics Technol. Lett.* **21**, 1594 (2009).
- J. Dai, M. Yang, X. Yu, K. Cao, and J. Liao, *Sens. Actuators, B* **174**, 253 (2012).
- S. Pevec and D. Donlagić, *Opt. Eng.* **58**, 1 (2019).
- B. Hopf, F. J. Dutz, T. Bosselmann, M. Willsch, A. W. Koch, and J. Roths, *Opt. Express* **26**, 12092 (2018).
- B. Hopf, B. Fischer, T. Bosselmann, A. W. Koch, and J. Roths, *Sensors* **19**, 144 (2019).
- G. Marchi, V. Stephan, F. J. Dutz, B. Hopf, L. Polz, H. P. Huber, and J. Roths, *J. Lightwave Technol.* **34**, 4557 (2016).
- Y. Sakamoto, T. Matsuo, H. Sakai, and T. B. Flanagan, *Zeitschrift für Physikalische Chemie* **162**, 83 (1989).
- F. Buchfellner, A. Stadler, Q. Bian, M. Hennesen, A. Zeisberger, A. W. Koch, and J. Roths, *Opt. Express* **30**, 44769 (2022).